Structure, stability, and spectra of lateral modes of a broad-area semiconductor laser

Blaaberg, Søren; Petersen, Paul Michael; Tromborg, Bjarne

Published in:
I E E E Journal of Quantum Electronics

Link to article, DOI:
10.1109/JQE.2007.904520

Publication date:
2007

Document Version
Publisher's PDF, also known as Version of record

Structure, Stability, and Spectra of Lateral Modes of a Broad-Area Semiconductor Laser

Søren Blaaberg, Paul Michael Petersen, and Bjarne Tromborg

***Abstract*—We present a theoretical analysis of the lateral modes of a broad-area semiconductor laser. The structure of the modes are classified into four categories and the modes are traced in the frequency versus pump rate diagram. It is shown how the branches of the frequency tuning curves for the different types of modes are interconnected and how the intensity profiles develop along the branches. The main result of the paper is the presentation of a small-signal stability analysis which identifies the saddle-node and Hopf bifurcation points on the mode tuning curves. For stable modes we derive expressions for small-signal noise and modulation spectra and present numerical examples of the spectra.**

***Index Terms*—Broad-area (BA) lasers, Green function, semiconductor lasers.**

I. Introduction

THE broad-area (BA) semiconductor laser is the simplest kind of laser diode to fabricate, and it is often used as a first step in laser fabrication to evaluate the quality of the epitaxial growth process and to characterize new epitaxial structures. The large active region enables high output power, but the spatial coherence of the output beam is usually poor due to poor lateral mode selectivity. For most applications the BA laser, therefore, has to be equipped with a mode selection mechanism before it is useful as high-power laser. The theme of this paper is a theoretical study of the static and dynamic properties of the BA stripe laser in its simplest form as depicted in Fig. 1. We address three main issues: 1) mapping of the diversity of lateral modes; 2) determination of their stability properties; and 3) calculation of noise and modulation spectra of stable modes.

The study was motivated by an attempt to understand and optimize the observed spatial coherence properties of a BA laser with asymmetric optical feedback from an external stripe mirror [1], [2]. Experiments show that when the stripe mirror reflects the field emitted in the junction plane at an angle θ relative to the optical axis, the output power emitted in the direction $-\theta$ is strongly enhanced and the field has strongly improved spatial coherence. The feedback supports asymmetric lateral modes of the solitary laser and an analysis of the configuration must, therefore, include a determination of these modes. (By modes we mean the stationary solutions to Helmholtz equation for the electric field and the rate equation for the carrier density in the slab waveguide of the BA laser, even though they are solutions to nonlinear systems of [3]). It seems that so far the problem of finding the modes of a solitary laser has only been partially solved [2]–[5]. Lang *et al.* [3] determined the symmetric modes by using the mean field approximation where the Helmholtz equation is reduced to a one-dimensional equation for the lateral modes by averaging the equation over the longitudinal coordinate. In [5], the symmetric modes were determined as functions of both the longitudinal and lateral coordinate, but the modes were only traced slightly above threshold due to numerical instabilities. The authors used a beam propagation method [6], which easily runs into numerical problems when the stationary solutions are closely spaced or saddle-node unstable. Wolff *et al.* [2] calculated the fundamental modes of the BA laser with asymmetric feedback from an external stripe mirror. For weak feedback and low pump currents these modes resemble asymmetric modes of the solitary laser, but they were not traced as stationary solutions for higher pump currents. In the present paper we use a modified version of the mean field approximation [3] and determine the lateral modes of our generic BA laser including both symmetric and asymmetric modes. A plot of the frequency versus pump rate tuning curves for the modes shows a complex and yet structured picture. We classify the modes into four groups and show how their tuning curves are interconnected and how the near- and far-field intensity profiles develop along the tuning curves.

The dynamic properties of the BA laser have been studied intensely over almost three decades, and time domain computer simulations have demonstrated a wide range of spatio-temporal nonlinear phenomena including chaotic behavior [7]–[16]. If the modes are stable they may be operating modes of the BA laser, and if they are unstable, they may still show up as attractors for the trajectories of the time domain solution in phase space. The experiments of Mailhot *et al.* [17] and Mandre *et al.* [18] show the presence of lateral modes even when the BA laser is not operating in a stationary state. The same behavior is seen in time domain computer simulations [13], [14].

A major part of this paper addresses the question of small-signal stability of the lateral modes. For a mode to be stable the zeros of the systems determinant have to lie in the upper half of the complex frequency plane. We follow the Green's function approach in [19] and present a derivation of the systems determinant for the combined carrier density rate equation and Helmholtz field equation in the mean field approximation. The determinant is used to identify saddle-node and Hopf bifurcation points on each of the mode tuning curves for our example structure. We had expected that the mechanism of self-stabilization [20], [21], which is of key importance for the stability of

Manuscript received April 18, 2007. The work of S. Blaaberg was supported in part by the Risø National Laboratory, Roskilde, Denmark.

S. Blaaberg and B. Tromborg are with COM-DTU, Department of Communications, Optics and Materials, Nano-DTU, Technical University of Denmark, Lyngby DK-2800, Denmark (e-mail: sbj@com.dtu.dk).

P. M. Petersen is with the Optics and Plasma Research Department, Risø National Laboratory, Roskilde DK-4000, Denmark (e-mail: paul.michael.petersen@risoe.dk).

Digital Object Identifier 10.1109/JQE.2007.904520

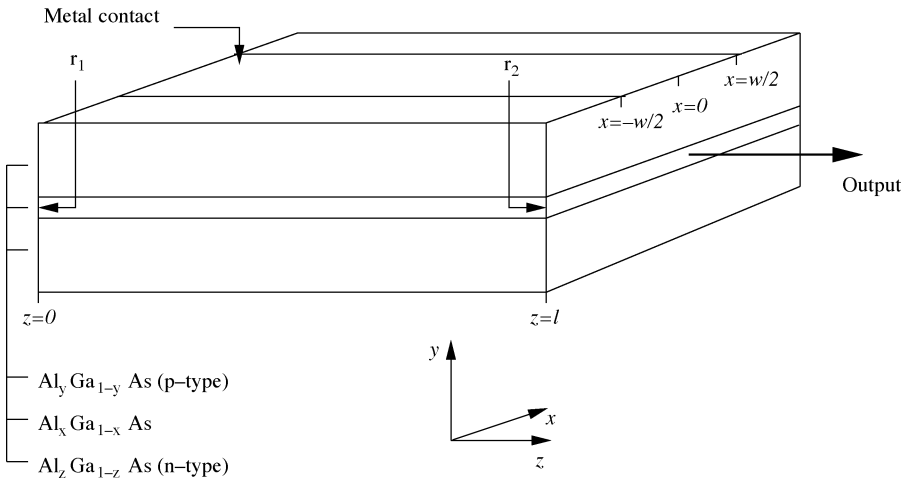

Fig. 1. Diagram of the BA laser. The origin of the coordinate system is centered in the middle of the waveguide at the back facet; it is shown displaced for clearness.

laser diodes in external cavity, would also ensure stability of several modes over an extended range of bias currents for BA lasers. However, for our example we find that only the lowest order mode is stable in the near-threshold region. Beyond this region the laser does not operate in a single lateral mode and a theoretical study of the dynamics must be pursued by other methods such as time domain computer simulations of the laser equations [7]–[16]. Alternative studies are presented in [22] and [23] where the stability of filaments are analyzed for BA lasers of infinite width.

The small-signal solution of the laser equations allows a calculation of the noise spectra of a stable mode. We derive expressions for the relative intensity noise (RIN) spectrum, the frequency noise spectrum and the field power spectrum, and present numerical calculations for our BA laser example. The spectra depend on the lateral position as was also demonstrated experimentally in [17] and [18].

The paper is organized as follows. Section II derives the basic equations based on the mean field approximation. Section III presents the lateral mode solutions with diagrams for the frequency tuning of the modes for increasing current pump rate. The small-signal analysis of the carrier rate equation and field equation in the mean field approximation is given in Section IV, and the stability properties of the modes are derived in Section V. The expressions for small-signal noise and current modulation spectra are derived in Section VI. The results and remaining issues are discussed in the final Section VII. Mathematical details are presented in four appendices.

II. Lateral Mode Equations for a BA Laser Diode

We consider a BA laser diode with the generic structure shown in Fig. 1. In the numerical calculations we assume the laser to have bulk gain region and the material composition to be GaAlAs–GaAs, but this is not essential for the theoretical analysis. The active layer is embedded in a separate confinement region that forms a slab waveguide. The width w of the top metal stripe contact is assumed to be less than the full width of the device such that laser operation is based on gain guiding and such that light interaction with the side walls can be ignored. On the other hand, we assume the stripe width to be large enough to allow several lateral modes between any two longitudinal modes. Close to the laser threshold the angular frequencies ω_{pm} of the stationary states are approximately given by $(n\omega_{pm}/c)^2 = (\pi p/l)^2 + (\pi m/w)^2$, where n is the modal refractive index, c is the vacuum light velocity, l is the length of the device, and p and m are the longitudinal and lateral mode numbers. The frequency detuning $\Delta\nu_m = (\omega_{pm} - \omega_{p1})/2\pi$ of the m-th lateral mode relative to the fundamental lateral mode $(m = 1)$ for fixed longitudinal mode number p is, therefore

$$\Delta\nu_m \simeq \frac{\lambda l}{4nw^2}(m^2 - 1)\Delta\nu_z \tag{1}$$

where λ is the lasing wavelength and $\Delta\nu_z$ is the frequency spacing of the longitudinal modes. In the numerical example we use the device parameters of Table I, which by (1) lead to about 25 lateral modes between two adjacent longitudinal modes.

TABLE I
List of Parameter Values

Parameter	Symbol	Value	Unit
Cavity length	l	1.0	mm
Stripe width	w	200	μm
Active layer thickness	h_a	0.2	μm
Linewidth enhancement factor	α	3.0	
Linear gain coefficient	a	1×10^{-20}	m^2
Confinement factor	Γ	0.3	
Effective refractive index	n_r	3.5	
Effective group index	n_g	4.0	
Reference wavelength	λ_r	810	nm
Transparency carrier density	N_0	1×10^{24}	m^{-3}
Internal loss	α_i	30	cm^{-1}
Mirror loss	α_m	10.05	cm^{-1}
Carrier lifetime	τ_c	5	ns

We assume the laser operates in a TE mode and that the lateral component of the frequency-domain electric field $\mathcal{E}(\mathbf{r},\omega)$ in the slap waveguide satisfies the Helmholtz equation

$$\left[\nabla^2 + k_0^2\epsilon(\mathbf{r},\omega)\right]\mathcal{E}(\mathbf{r},\omega) = F(\mathbf{r},\omega). \tag{2}$$

$F(\mathbf{r},\omega)$ is a Langevin noise function that describes the spontaneous emission noise, $\epsilon(\mathbf{r},\omega)$ is the (complex) dielectric con-

stant, and $k_0 = \omega/c$ is the vacuum vavenumber. Furthermore, we assume that the field is of the form

$$\mathcal{E}(x,y,z,\omega) = E_\omega^+(x,z)\phi(y)e^{-j\beta z} + E_\omega^-(x,z)\phi(y)e^{j\beta z}. \quad (3)$$

The orientation of the xyz axes are as shown in Fig. 1. $E_\omega^+(x,z)$ and $E_\omega^-(x,z)$ are field envelopes describing forward and backward travelling waves in the longitudinal direction. They are assumed to be slowly varying functions of z. The function $\phi(y)$ describes the transverse field distribution and is taken to be normalized to unity, i.e $\int |\phi(y)|^2 dy = 1$.

Our aim is to study the structure of lateral modes for a given longitudinal mode. We shall, therefore, assume that β in (3) is the solution to the oscillation condition

$$r_1 r_2 \exp(-2j\beta l) = 1 \quad (4)$$

with longitudinal mode number p, i.e.,

$$\beta = \frac{\pi p}{l} + \frac{j}{2}\alpha_m \quad (5)$$

where r_1 and r_2 are the back and front facet reflectivities, and $\alpha_m = -ln(r_1 r_2)/l$ is the distributed mirror loss.

In Appendix A we show how the problem of solving the 3-dimensional scalar wave equation (2) can be reduced to solving a 1-dimensional wave equation by applying a weighted mean field approximation. The resulting wave equation is

$$\left[\frac{\partial^2}{\partial x^2} + k^2 - \beta^2\right] E_\omega(x) = f_\omega(x) \quad (6)$$

where $E_\omega(x)$ and $f_\omega(x)$ are field and noise functions obtained by performing a weighted average over the z coordinate. They are given by (60) and (61) in Appendix A.

The wave equation is identical to the equation used by a number of authors (see, e.g., [3] and [4]), but our definition of the mean field deviates from the previous definitions when the facet reflectivities deviate from unity. The participation of more than one longitudinal mode in the dynamics of the BA laser may be taken into account by introducing a field equation like (6) for each of the longitudinal modes. However, here we assume that only one longitudinal mode is active.

The average complex wave number k in (6) is written in the usual form as

$$k = \frac{\omega n}{c} + \frac{j}{2}(g - \alpha_i) \quad (7)$$

where n is the modal index, g is the modal gain and α_i is the internal loss, all averaged over z. Both n and g are functions of the longitudinally averaged carrier density $N(x)$. For g, we simply assume the linear behavior

$$g = \Gamma a(N - N_0) \quad (8)$$

where N_0 is the carrier density at transparency, Γ is the transverse confinement factor and a is the differential material gain. We shall use the set (N_r, ω_r) for which $k(N_r, \omega_r) = \pi p/l \equiv k_r$ as reference carrier density and reference frequency around which we expand $k(N,\omega)$

$$k(N,\omega) = k_r + \frac{\partial k}{\partial \omega}(\omega - \omega_r) + \frac{\partial k}{\partial N}(N(x) - N_r). \quad (9)$$

For the partial derivatives of k, we use

$$\frac{\partial k}{\partial \omega} = \frac{n_g}{c} = \frac{1}{v_g}, \quad \frac{\partial k}{\partial N} = (j - \alpha)\frac{\Gamma a}{2} \quad (10)$$

where n_g is the group index, v_g is the group velocity, and α is the linewidth enhancement factor.

The frequency domain field (6) can be transformed to a time domain field equation for the complex field envelope $E(x,t)$ defined by

$$E(x,t)e^{j\omega_s t} = \frac{1}{2\pi}\int_0^\infty E_\omega(x)e^{j\omega t}d\omega \quad (11)$$

where ω_s is the optical frequency of the lateral mode under consideration. Inserting (9) in (6) and using the transformation (11), the field equation becomes

$$\left[\frac{\partial^2}{\partial x^2} - j\frac{2k_r}{v_g}\frac{\partial}{\partial t} + \kappa(x,t)\right] E(x,t) = f(x,t) \quad (12)$$

where

$$\kappa(x,t) = 2k_r\left[\frac{1}{v_g}(\omega_s - \omega_r) + \frac{\partial k}{\partial N}(N(x,t) - N_r) - j\frac{\alpha_m}{2}\right]. \quad (13)$$

The noise function $f(x,t)$ is obtained from $f_\omega(x)$ by a transformation similar to (11).

The field (12) has to be supplemented with the carrier density rate equation. In the time domain it reads

$$\frac{\partial}{\partial t}N(x,t) = J(x,t) - \frac{N(x,t)}{\tau_c} - \frac{v_g}{\Gamma}g(x,t)S(x,t) \quad (14)$$

where $J(x,t)$ is the pumping term, τ_c is the carrier lifetime, and $S(x,t)$ is the photon density in the active layer. The relation between $S(x,t)$ and $E(x,t)$ is given in (62). In the present study we ignore effects of carrier diffusion and carrier noise due to pumping and carrier recombination.

We assume that the pump current is the sum $J(x,t) = J_s(x) + \delta J(x,t)$ of a stationary pump current $J_s(x)$ and a small modulation term $\delta J(x,t)$. The current $J_s(x)$ is assumed to be stationary and uniform under the metal contact, and we model the current spreading at the metal edges by an exponential decay in regions of width d_0 outside the contacts. Thus

$$J_s(x) = \begin{cases} J_0 \exp\left((x + w/2)/d_0\right), & \text{for } x < -w/2 \\ J_0, & \text{for } |x| < w/2 \\ J_0 \exp\left(-(x - w/2)/d_0\right), & \text{for } x > w/2. \end{cases} \quad (15)$$

The actual current spreading in a given device depends on detailed epitaxial structure and can be calculated by solving Poisson's equation in the transverse plane [24], but as discussed in [3] the model (15) is a reasonable approximation. We shall consider the two cases, $d_0 = 0$ and $d_0 = 10\ \mu$m.

The steady-state field and carrier distributions, $E(x,t) = E_s(x)$ and $N(x,t) = N_s(x)$, for the stationary lateral modes are obtained as solutions to (12) and (14) for $J = J_s$ and for noise driving term $f(x,t) = 0$. The carrier rate (14) gives the relation

$$N_s(x) - N_0 = \frac{J_s(x)\tau_c - N_0}{1 + |E_s(x)|^2 / P_{\text{sat}}} \tag{16}$$

where by (62) the saturation parameter P_{sat} is

$$P_{\text{sat}} = \frac{\hbar\omega h_a}{2\epsilon_0 nc\Gamma a\tau_c K}. \tag{17}$$

The field equation for the stationary lateral modes $E_s(x)$ is then obtained by neglecting the noise term $f(x,t)$ in (12) and using the expression (16) for the stationary carrier density in (13). The resulting single nonlinear differential equation reads

$$\left[\frac{\partial^2}{\partial x^2} + \kappa_s(x)\right] E_s(x) = 0 \tag{18}$$

where

$$\kappa_s(x) = 2k_r \left[\frac{1}{v_g}(\omega_s - \omega_r) + \frac{\partial k}{\partial N}\frac{J_s(x)\tau_c - N_0}{1 + |E_s(x)|^2 / P_{\text{sat}}} - \frac{\alpha_i}{2}(j - \alpha) - j\frac{\alpha_m}{2}\right]. \tag{19}$$

The stationary lateral modes are the solutions to (18) which vanishes for $|x| \gg w/2$, i.e., solutions for which the dependence of $\kappa_s(x)$ on $|E_s(x)|^2$ can be ignored for large $|x|$. Since $\text{Im}(\kappa_s)$ approaches the negative value, $-k_r(\Gamma a N_0 + \alpha_i + \alpha_m)$, for $|x| \to \infty$, the modes must satisfy the boundary conditions

$$\frac{d}{dx}\ln E_s \to \mp j\sqrt{\kappa_s}\,, \quad \text{for } x \to \pm\infty. \tag{20}$$

The conditions can only be met for discrete values of ω_s.

III. Structure of the Stationary Lateral Modes

In this section, we show that for pump currents up to about 20% above threshold, the set of stationary solutions to (18) can be categorized into a few well-defined types. For higher pump currents, the set becomes increasingly more complicated due to the nonlinearity of the equation. In our example of a BA laser with bulk active layer, the transparency current is high and, therefore, nonlinear effects become important already about 1% above threshold. (For a quantum-well device with low transparency current, the nonlinear effects will typically show up at about 10% above threshold [3]). As we show in Section V, all stationary solutions become unstable slightly above threshold, and the laser will, therefore, usually operate in a chaotic attractor state for currents well above threshold unless a particular solution is made stable, e.g., by filtered optical feedback or by tailoring the current distribution $J_s(x)$.

The lateral symmetry of the laser structure and injection current ensures that for any solution $\{E_s(x), N_s(x), \omega_s\}$, the reflected set $\{E_s(-x), N_s(-x), \omega_s\}$ is also a solution. In the linear regime near threshold where $|E_s|^2 \ll P_{\text{sat}}$, the field solutions are either even ($E_s(x) = E_s(-x)$) or odd ($E_s(x) = -E_s(-x)$), but at higher pump rates the nonlinearity results in asymmetric field solutions with no definite parity.

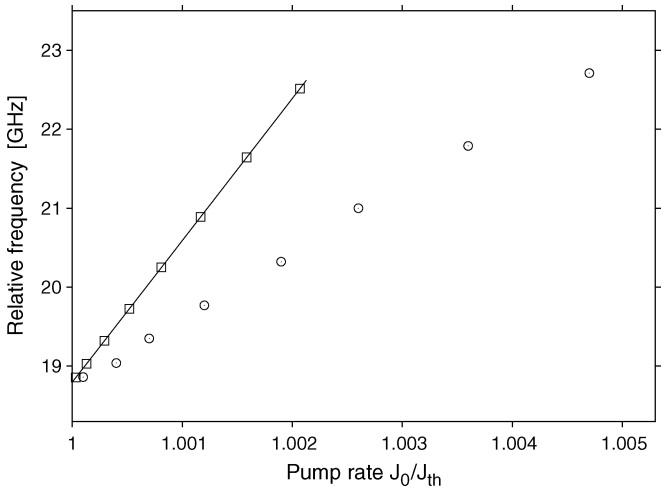

Fig. 2. Threshold frequencies for $d_0 = 0$ (squares) and $d_0 = 10\,\mu$m (open circles). The solid line is given by the equation obtained by taking the norm on both sides of (21).

The threshold values of frequency and pump rate are found by solving (18) in the linear regime where $|E_s|^2 \ll P_{\text{sat}}$. For the example with $d_0 = 0$, i.e., $J_s(x) = 0$ for $|x| > w/2$, the problem reduces to solving the simple complex transcendental equations

$$e^{j2\sqrt{\kappa_1}w} = \left(\frac{\sqrt{\kappa_1} - \sqrt{\kappa_2}}{\sqrt{\kappa_1} + \sqrt{\kappa_2}}\right)^2 \tag{21}$$

where κ_1 and κ_2 are given by κ_s for $J(x) = J_0$ and $J(x) = 0$, respectively, and for infinite P_{sat}. It follows from the derivation of (21) that the solution $\kappa_1 = 0$, is a false solution to the problem. Fig. 2 compares the relative frequencies $\nu_s = (\omega_s - \omega_0)/(2\pi)$ derived from (21) with the frequencies obtained by direct solution of (18) in the linear regime using $d_0 = 10\,\mu$m. The horizontal axis is the relative pump rate J_0/J_{th}, where

$$J_{\text{th}} \equiv \frac{1}{\tau_c}\left(N_0 + \frac{\alpha_i + \alpha_m}{\Gamma a}\right) \tag{22}$$

is close to the threshold pump rate of the fundamental lateral mode for both examples of d_0. In both cases the threshold frequencies increase almost linearly with threshold current and quadratically with mode number. The latter is expected from the simple relation (1). The increase of threshold current with lateral mode number is qualitatively explained by the deeper penetration of modes into the absorbing region outside the metal contact for increasing mode number [3]. This effect is somewhat more pronounced for $d_0 = 10\,\mu$m than for $d_0 = 0$.

For the rest of this section we shall only consider the case $d_0 = 10\,\mu$m. Fig. 3 presents calculated frequency tuning curves, ν_s versus J_0/J_{th}, and Figs. 4 and 5 show excerpts from Fig. 3 for clarity. We categorize the lateral mode solutions in Figs. 3–5 into three different types corresponding to different branches of the tuning curves. We have also identified a fourth type of modes with tuning curves that partly overlap the curves in Fig. 3. They are shown separately in Fig. 6 for clarity. All modes have

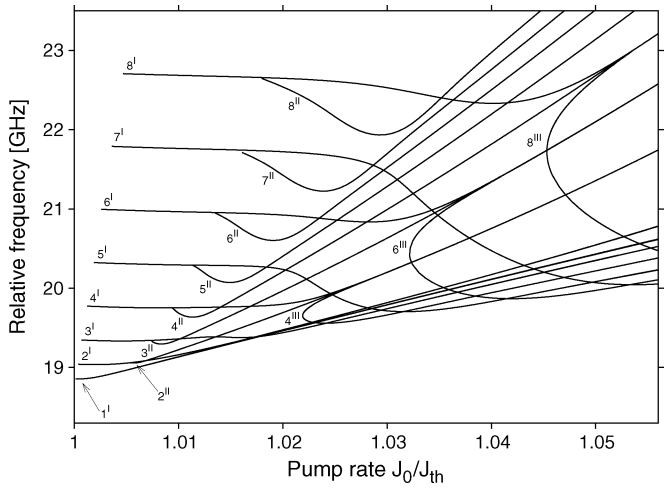

Fig. 3. Frequency tuning curves ν_s versus $J_0/J_{\rm th}$ for modes $m^{\rm I}$, $m^{\rm II}$ and $m^{\rm III}$ for $m = 1$ to $m = 8$.

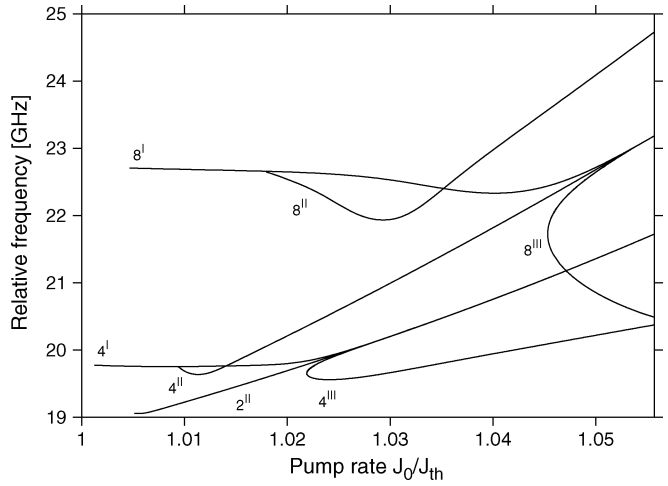

Fig. 4. Excerpt from Fig. 3 showing tuning curves for modes m =2, 4 and 8.

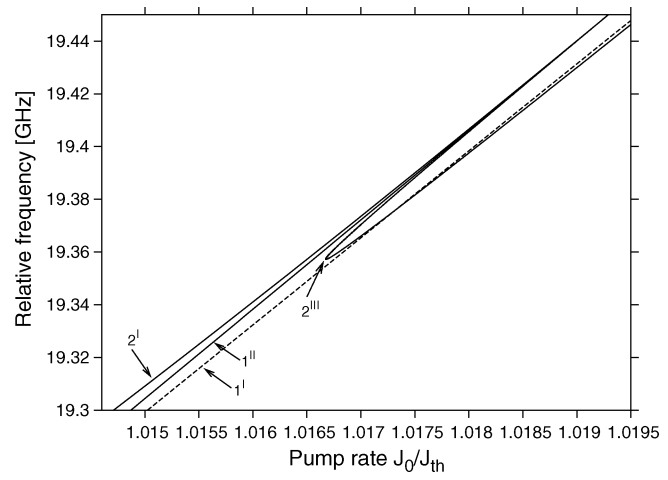

Fig. 5. Excerpt from Fig. 3 showing the merger of modes $1^{\rm II}$, $2^{\rm I}$, and $2^{\rm III}$.

near-field intensity distributions where the number of peaks are given by their lateral mode number.

a) Type I Modes: Modes of type I are the modes of definite parity, which evolve from the threshold solutions. They are

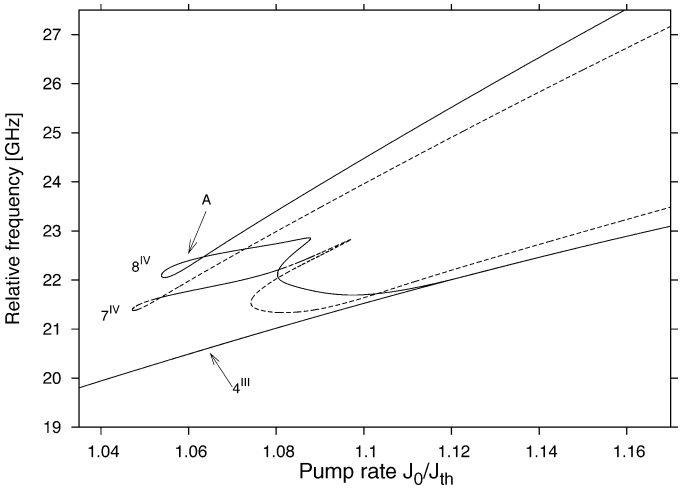

Fig. 6. Tuning curves of modes $4^{\rm III}$, $7^{\rm IV}$, and $8^{\rm IV}$.

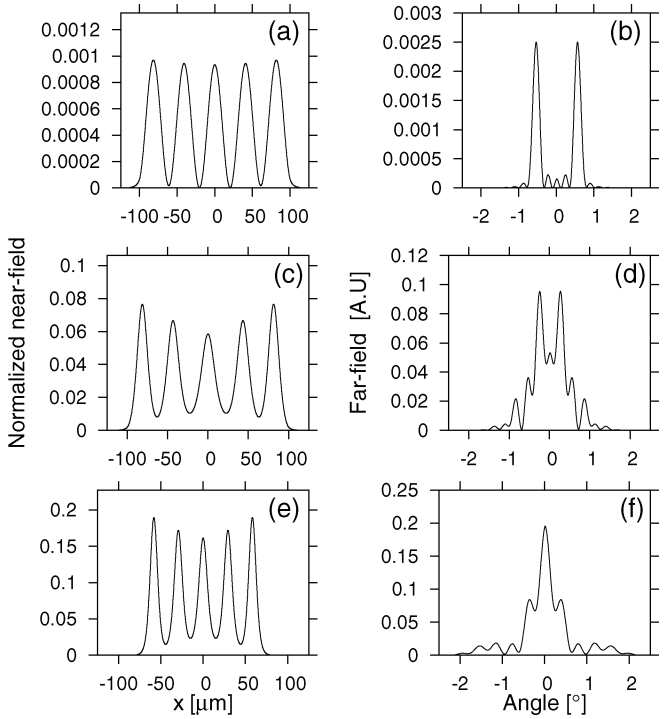

Fig. 7. Normalized near-field, $|E_s(x)|^2/P_{\rm sat}$, and far-field profiles for mode $5^{\rm I}$ and $J_0/J_{\rm th}$ = (a) and (b) 1.0022, (c) and (d) 1.0274, (e) and (f) 1.0665 .

labelled $m^{\rm I}$ by their lateral mode number m, and they have even (odd) field solutions $E_s(x)$ for odd (even) m. The frequencies of the modes stay almost constant with pump rate until nonlinear effects become important and new branches emerge on the lower side of the tuning curves. These branches, labelled $m^{\rm II}$, are tuning curves of the second kind of modes to be described below. The evolution of the modes of type I depends qualitatively on their parity. Fig. 7 show the evolution of the near- and far-field intensity distributions for $m = 5$ for increasing levels of pump rate ($J_0/J_{\rm th}$ = 1.0022, 1.0274, 1.0665). The near-field intensity profile is seen to be depleted near the edges of the metal contact as the pump rate is increased and the initial twin-loped structure of the far-field is evolving into a distorted single lope. Fig. 8 show the corresponding evolution for $m = 4$ and for $J_0/J_{\rm th}$ =1.00156, 1.019, and

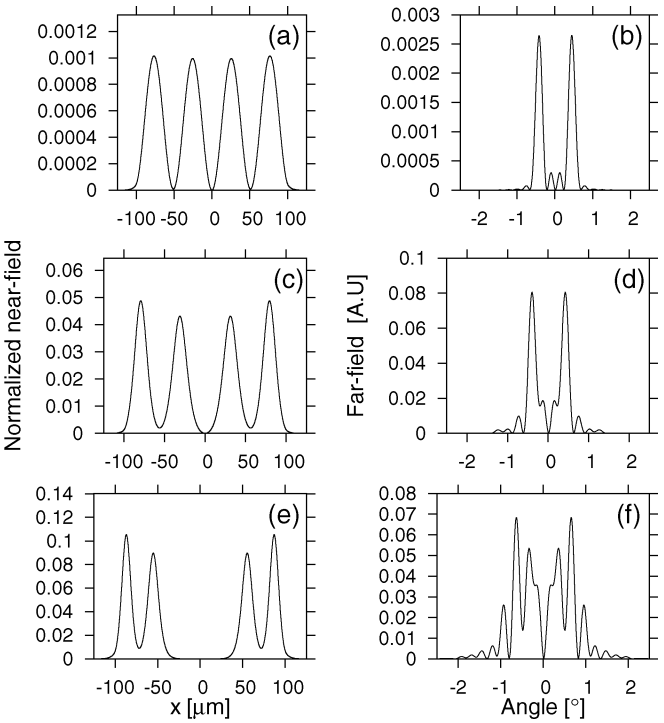

Fig. 8. Normalized near-field, $|E_s(x)|^2/P_{\rm sat}$, and far-field profiles for mode $4^{\rm I}$ and $J_0/J_{\rm th}=$ (a) and (b) 1.00156, (c) and (d) 1.019, (e) and (f) 1.041.

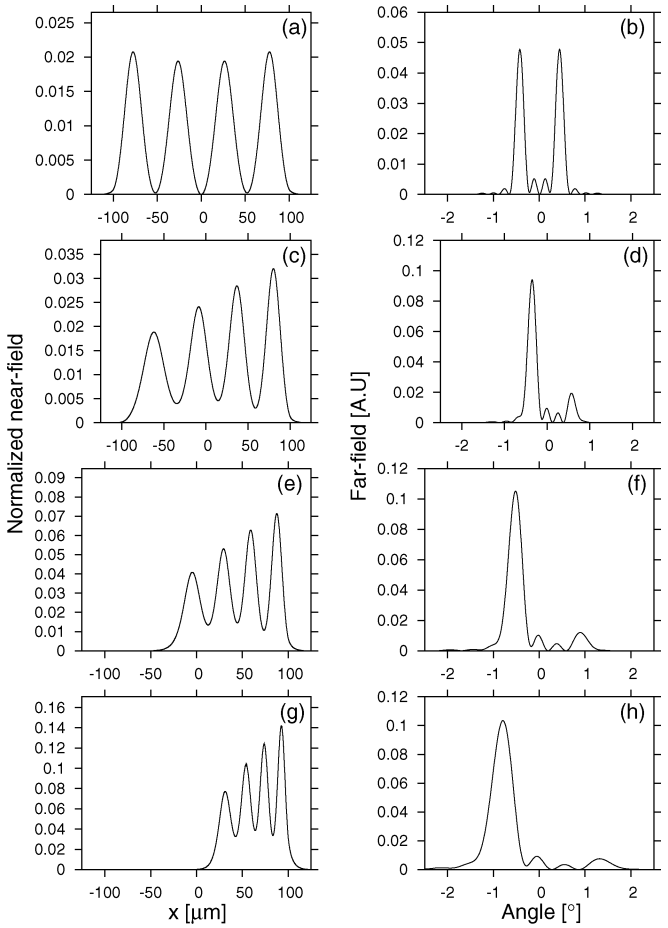

Fig. 9. Normalized near-field and far-field profiles for mode $4^{\rm II}$ and $J_0/J_{\rm th}=$ (a) and (b) 1.0093, (c) and (d) 1.011, (e) and (f) 1.025, (g) and (h) 1.053.

1.041. In this case the near field develops a hole at the center and increased intensity around $x=\pm w/2$, and the far-field remains twin-loped although increasingly distorted.

b) Type II Modes: The modes of type II are frequency degenerate, so for each point on the $m^{\rm II}$ tuning curve there are two solutions, $E_s(x)$ and $E_s(-x)$. For each m the two modes of type II are created in a saddle-node bifurcation from the $m^{\rm I}$ mode, and as seen from Figs. 3–5 the tuning curve of $m^{\rm II}$ eventually merges with the tuning curve of $(2m)^{\rm I}$. The field distributions of the $m^{\rm I}$ and $m^{\rm II}$ modes coincide at the bifurcation point, but for increasing current the intensity distributions of the $m^{\rm II}$ modes become increasingly asymmetric and concentrated on the positive or negative x-axis. The evolution of the near- and far- field distributions is shown for $m=4$ in Fig. 9. The far-field shows a gradual change from a twin lobed to a single lobe pattern. At the point where the $4^{\rm II}$ tuning curve merges with $8^{\rm I}$, the fields of the two $4^{\rm II}$ solutions are vanishingly small on either the positive or negative x axis and on the other half-axes their near field intensity distributions coincide with the intensity distribution of the $8^{\rm I}$ solution. A qualitatively similar behavior is seen for the other type II tuning curves. If carrier diffusion is included in the model, the merger of $m^{\rm II}$ and $(2m)^{\rm I}$ tuning curves will only be approximate.

c) Modes of Type III and IV: In addition to modes of type I and type II, Figs. 3–5 show tuning curves labelled $m^{\rm III}$. These solutions also correspond to asymmetric field distributions and are double degenerate like the type II solutions. For even m, the $m^{\rm III}$ tuning curve starts from the point where the tuning curve $m^{\rm I}$ merges with $(m/2)^{\rm II}$, and here the intensity distributions of $m^{\rm I}$ and $m^{\rm III}$ are identical. For odd m, the type III curves are not visible in the figure as they lie very close to their type I "parents." They start off tangential to their respective type I parent pointing towards higher pump rates, i.e., they do not have turning points like the type III curves for even m. Furthermore, we have found no mode of type $1^{\rm III}$. The near- and far-field distributions of $4^{\rm III}$ solutions are shown in Fig. 10 for four points on the tuning curve. The first [Fig. 10(a) and (b)] is at the starting point at $J_0/J_{\rm th}=1.029$, and the second [Fig. 10(c) and (d)] is at the foremost left point of the tuning curve. For points on the lower part of the $4^{\rm III}$ tuning curve, the near-field intensity distribution becomes increasingly asymmetric with increasing current as shown in Fig. 10(e) and 10(g). At the last point [Fig. 10(g) and (h)], the tuning curve of $4^{\rm III}$ merges with yet another type of mode, $8^{\rm IV}$, as shown in Fig. 6. This type of mode is of definite parity; the near- and far-field intensity distributions are shown in Fig. 11 for the point labelled "A" in Fig. 11 and for the point where $8^{\rm IV}$ merges with $4^{\rm III}$. The near-field distribution in Fig. 11(c) coincides with the distribution in Fig. 10(g) for $x\le 0$. Fig. 6 also shows the tuning curve of $7^{\rm IV}$, which is not connected to modes at lower pump rate. Both type IV tuning curves show a complex behavior with a loop and a cusp. We have not made a systematic search for other modes of type IV so we cannot be sure that they actually exist.

In summary, Figs. 3–5 show tuning curves for type I (definite parity), type II (asymmetric), and type III (asymmetric) for $m=1$ to $m=8$. For increasing pump rate the near-field intensity

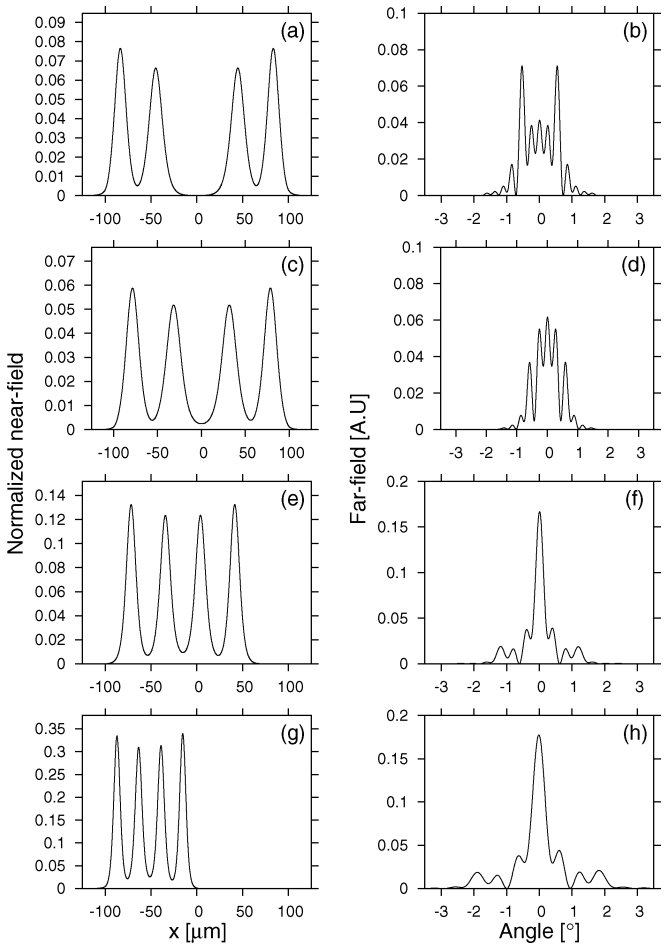

Fig. 10. Normalized near-field and far-field profiles for mode 4^{III} at the start of the branch at (a) and (b) $J_0 = 1.029\,J_{\mathrm{th}}$, at the turning point at (c) and (d) $J_0 = 1.022\,J_{\mathrm{th}}$, at (e) and (f) $J_0 = 1.048\,J_{\mathrm{th}}$, and at (g) and (h) $J_0 = 1.12\,J_{\mathrm{th}}$, where 4^{III} merges with 8^{IV}.

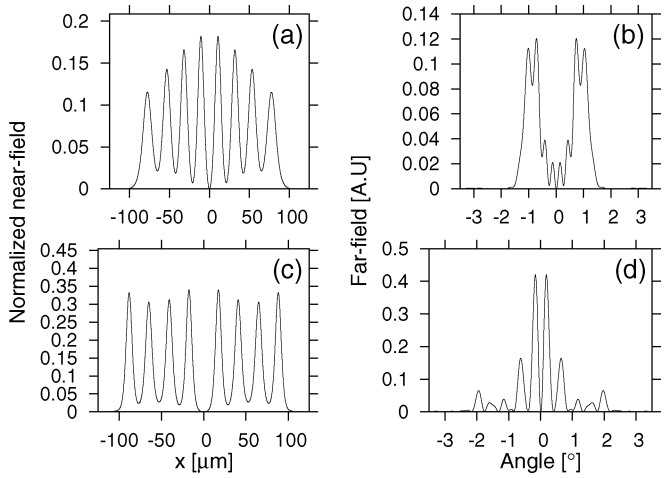

Fig. 11. Normalized near-field and far-field profiles for mode 8^{IV} at the point labelled A in Fig. 6 [(a) and (b)] and at the point where 8^{IV} merges with 4^{III} [(c) and (d)].

distributions of type II and type III tend to become localized on the intervals $[-w/2, 0]$ or $[0, w/2]$ on the x-axis. The envelopes of the type II distributions are tilted with maximum near the edge of the metal contact, while the envelopes of the type III distributions are almost constant.

IV. Small-Signal Analysis of Lateral Modes

If the stationary solution given by the set $\{\omega_s, E_s(x), N_s(x)\}$ is stable, the field and carrier density (12) and (14) can be solved to first-order in the noise function $f(x,t)$. In this section we derive the semianalytical expressions for the solutions.

It is convenient to rewrite the field (12) as an equation for the logarithmic field, $h = \ln E = \ln a + j\phi$, where $a = |E|$ and ϕ is the phase of E

$$\frac{\partial^2}{\partial x^2}h + \left(\frac{\partial}{\partial x}h\right)^2 - j\frac{2k_r}{v_g}\frac{\partial}{\partial t}h + \kappa = \frac{f}{E}. \tag{23}$$

The first-order deviations of h, E, a, ϕ, N from their stationary solutions h_s, E_s, a_s, ϕ_s, N_s are denoted by δh, δE, δa, $\delta\phi$, δN. We obtain an equation for $\delta h = \delta E/E_s = \delta a/a_s + j\delta\phi$ by taking the differential of (23)

$$\frac{\partial^2}{\partial x^2}\delta h + 2\left(\frac{d}{dx}h_s\right)\left(\frac{\partial}{\partial x}\delta h\right) - j\frac{2k_r}{v_g}\frac{\partial}{\partial t}\delta h + \delta\kappa = \frac{f(x,t)}{E_s(x)} \tag{24}$$

where the differential $\delta\kappa$ is

$$\delta\kappa(x,t) = 2k_r\frac{\partial k}{\partial N}\delta N(x,t). \tag{25}$$

By splitting (24) into real and imaginary parts, it can be written as the vector equation

$$\frac{\partial^2}{\partial x^2}\boldsymbol{\psi} + \boldsymbol{M}_1\frac{\partial}{\partial x}\boldsymbol{\psi} + \boldsymbol{M}_2\frac{\partial}{\partial t}\boldsymbol{\psi} + k_r\Gamma a\delta N\begin{pmatrix}-\alpha\\1\end{pmatrix} = \boldsymbol{f} \tag{26}$$

for the vector

$$\boldsymbol{\psi} = \begin{pmatrix}\mathrm{Re}(\delta h)\\ \mathrm{Im}(\delta h)\end{pmatrix} = \frac{1}{a_s}\begin{pmatrix}\delta a\\ a_s\delta\phi\end{pmatrix}. \tag{27}$$

The 2×2 matrices $\boldsymbol{M}_1$ and $\boldsymbol{M}_2$ are

$$\boldsymbol{M}_1 = 2\frac{d}{dx}\begin{pmatrix}\mathrm{Re}\,h_s & -\mathrm{Im}\,h_s\\ \mathrm{Im}\,h_s & \mathrm{Re}\,h_s\end{pmatrix}$$
$$\boldsymbol{M}_2 = \frac{2k_r}{v_g}\begin{pmatrix}0 & 1\\ -1 & 0\end{pmatrix} \tag{28}$$

and the noise driving term is

$$\boldsymbol{f} = \frac{1}{|E_s|^2}\begin{pmatrix}\mathrm{Re}\,(fE_s^*)\\ \mathrm{Im}\,(fE_s^*)\end{pmatrix}. \tag{29}$$

The first-order deviation in carrier density, δN, is found from (14) to be

$$\frac{\partial}{\partial t}\delta N = \delta J(x,t) - \frac{\delta N}{\tau_c} - \frac{|E_s|^2}{\tau_c P_{\mathrm{sat}}}\left[\delta N + 2(N_s - N_0)\mathrm{Re}(\delta h)\right]. \tag{30}$$

By taking the Fourier transform of (26) and (30), the two equations can be combined to a single linear equation

$$\left[\frac{d^2}{dx^2} + \boldsymbol{M}_1\frac{d}{dx} + \boldsymbol{M}\right]\widetilde{\boldsymbol{\psi}} = \widetilde{\boldsymbol{f}} + \widetilde{\boldsymbol{j}} \tag{31}$$

for the Fourier transform $\widetilde{\boldsymbol{\psi}}(x,s)$ of $\boldsymbol{\psi}(x,t)$. The Laplace variable s is related to the baseband frequency Ω by $s = j\Omega$. A tilde

over a symbol indicates that it is a function in the baseband frequency domain. The matrix $\boldsymbol{M}$ is given by

$$\boldsymbol{M} = \boldsymbol{M}_0 + s\boldsymbol{M}_2 \tag{32}$$

where

$$\boldsymbol{M}_0 = 2k_r\Gamma a \frac{(N_s(x) - N_0)\,|E_s|^2/P_{\rm sat}}{1 + s\tau_c + |E_s|^2/P_{\rm sat}} \begin{pmatrix} \alpha & 0 \\ -1 & 0 \end{pmatrix}. \tag{33}$$

The noise driving term $\widetilde{\boldsymbol{f}}$ is the baseband Fourier transform of $\boldsymbol{f}$ and $\widetilde{\boldsymbol{j}}$ is the current modulation term

$$\widetilde{\boldsymbol{j}} = \frac{k_r\Gamma a\tau_c \widetilde{\delta J}(x,s)}{1 + s\tau_c + |E_s(x)|^2/P_{\rm sat}} \begin{pmatrix} \alpha \\ -1 \end{pmatrix}. \tag{34}$$

The linear differential equation (31) can be solved by a Green's function method. In analogy with the procedure in [19] we introduce the Green's function $\boldsymbol{\zeta}_i(x, x_0, s)$ which satisfies the equation

$$\frac{d^2}{dx^2}\boldsymbol{\zeta}_i - \frac{d}{dx}\left(\boldsymbol{M}_1^\dagger \boldsymbol{\zeta}_i\right) + \boldsymbol{M}^\dagger \boldsymbol{\zeta}_i = \hat{\boldsymbol{e}}_i \delta(x - x_0) \tag{35}$$

for $i = 1, 2$, and where the unit vectors $\hat{\boldsymbol{e}}_i$ have components $(\hat{\boldsymbol{e}}_i)_j = \delta_{ij}$, $j = 1, 2$. The symbol "†" means Hermitian conjugate. Multiplying (31) from the left by $\boldsymbol{\zeta}_i^\dagger$ and integrating with respect to x over the interval $[-d, d]$ lead by partial integration to the solution

$$\left(\widetilde{\boldsymbol{\psi}}(x_0, s)\right)_i = \int_{-d}^{d} \boldsymbol{\zeta}_i^\dagger(x, x_0, s)\left[\widetilde{\boldsymbol{f}}(x,s) + \widetilde{\boldsymbol{j}}(x,s)\right] dx \tag{36}$$

provided $\boldsymbol{\zeta}_i(x, x_0, s)$ satisfies the boundary conditions

$$\frac{d}{dx}\boldsymbol{\zeta}_i(x, x_0, s) = \boldsymbol{M}_1^\dagger(x)\boldsymbol{\zeta}_i(x, x_0, s) \tag{37}$$

for $x = \pm d$. Furthermore, the integration interval $[-d, d]$ has to be chosen with $d > w/2 + d_0$ such that we can assume $d\widetilde{\boldsymbol{\psi}}/dx = 0$ for $x = \pm d$. In Appendix B we show how to calculate the Green's function $\boldsymbol{\zeta}_i(x, x_0, s)$ and also the systems determinant $D(s)$ which determines the stability properties of the mode.

Since $(\widetilde{\boldsymbol{\psi}}(x,s))_1 = \widetilde{\delta a}(x,s)/a_s(x)$ and $(\widetilde{\boldsymbol{\psi}}(x,s))_2 = \widetilde{\delta\phi}(x,s)$ the solution (36) allows a calculation of the amplitude and phase noise spectra as will be demonstrated in Section VI.

V. Stability Properties of the Lateral Modes

The stability of a lateral mode is determined by the location of zeros of the system determinant $D(s)$ in the complex s-plane. The mode is unstable if $D(s)$ has one or more zeros in the right-half s-plane, i.e., zeros with positive real part. Since $D^*(s) = D(s^*)$, the zeros appear as complex-conjugate pairs unless they lie on the real axis. The occurrence of instability may be associated with a complex-conjugate pair of zeros moving into the right-half s-plane as a control parameter is changed. In that case the considered mode (fixed-point solution) performs a Hopf bifurcation where it bifurcates into an unstable fixed-point and a stable limit cycle. Alternatively, the instability may occur when a zero moves into the right-half s-plane along the real axis. The corresponding bifurcation is of the saddle-node type where a stable and an unstable fixed point are created or annihilated. In our case we use the pump rate as control parameter and study the location of zeros as the pump rate is increased.

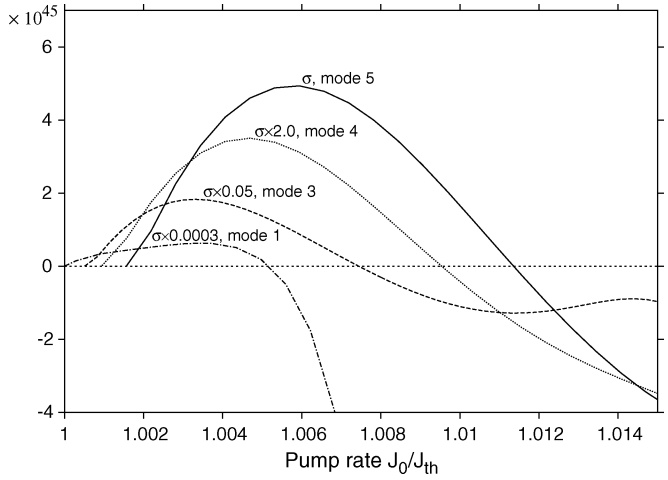

Fig. 12. Stability parameter σ versus pump rate for modes $1^{\rm I}$, $3^{\rm I}$, $4^{\rm I}$ and $5^{\rm I}$. The zero crossings mark the position of saddle-node bifurcation points.

As shown in Appendix C, the system determinant $D(s)$ has a fixed zero at $s = 0$. The passage of a zero of $D(s)$ through $s = 0$ along the real axis for changing pump rate can, therefore, be identified by the derivative of $D(s)$ at $s = 0$ being zero at the bifurcation point. This suggests that the derivative $\sigma \equiv dD/ds(s = 0)$ is used as a stability parameter. It can be shown that $D(s)$ increases exponentially for $s \to \infty$ along the real axis, so a negative σ implies that there are one or more zeros of $D(s)$ on the positive real s-axis, i.e., the mode is unstable. If on the other hand σ is positive, one can only conclude that there are no zeros or an even number of zeros on the positive real axis. One can check numerically that the type I modes have no zeros on the positive real axis for pump rates slightly above threshold. The σ-parameter is, therefore, positive just above threshold, and by calculating σ as a function of the pump rate one can determine the bifurcation point where the type II branch is created. This is illustrated in Fig. 12 which shows σ as a function of pump rate for modes $1^{\rm I}$, $3^{\rm I}$, $4^{\rm I}$, and $5^{\rm I}$. The pump rate positions of the branching points of type II modes are given by the zeros of σ. The type I modes are unstable with negative σ above the branch point, while type II modes have positive σ at least in the vicinity of the branch point. Extending the calculations of σ for mode $5^{\rm I}$ to higher pump rates (not shown) we find that σ becomes positive again at the bifurcation point $(J_0/J_{\rm th} = 1.047)$ where mode $5^{\rm III}$ is created.

In a detailed study of Hopf bifurcations one may locate the off axis zeros of $D(s)$ and trace their trajectories in the complex s-plane for increasing pump rate. However, if we are only interested in deciding whether or when the zeros are in the right-half

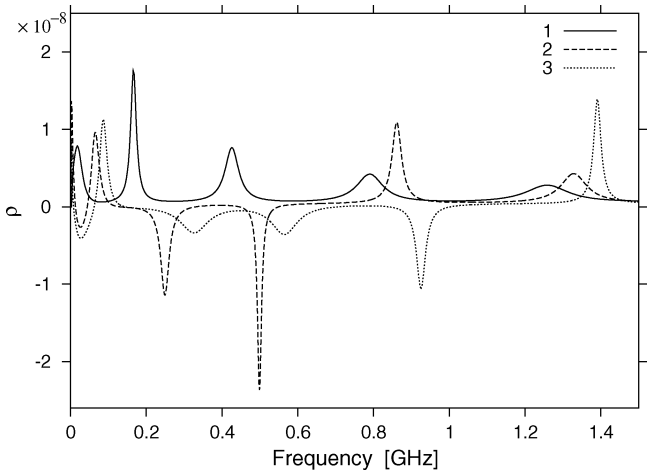

Fig. 13. Function $\rho(\Omega)$ defined in (39) for the fundamental mode 1^{I}. Shown versus $\Omega/2\pi$ for J_0/J_{th} =1.00028 (solid), 1.00153 (dashed), and 1.00247 (dotted).

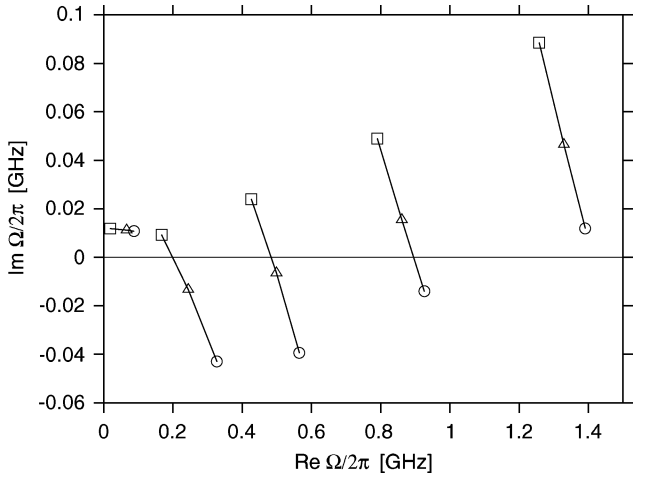

Fig. 14. Zeros of the systems determinant $D(s)$ in the complex frequency plane for the same pump rates as in Fig. 13. J_0/J_{th} =1.00028 (squares), 1.00153 (triangles), and 1.00247 (open circles). The interconnecting lines are shown to guide the eye.

s-plane there is a simpler approach. For s close to a zero s_0 of $D(s)$, we can expand $D(s)$ as

$$D(s) \simeq a(s - s_0). \tag{38}$$

For $s = j\Omega$ the function $\rho(\Omega)$ defined by

$$\rho(\Omega) \equiv \mathrm{Re}\left(\frac{1}{D(s)}\frac{d}{ds}D(s)\right) \tag{39}$$

will, therefore, have the Lorentzian form

$$\rho(\Omega) \simeq -\frac{\mathrm{Re}(s_0)}{(\Omega - \mathrm{Im}(s_0))^2 + (\mathrm{Re}(s_0))^2} \tag{40}$$

for $\Omega \simeq \mathrm{Im}(s_0)$. In a plot of ρ versus Ω, a zero close to the imaginary axis in the s-plane will, therefore, show up as a positive peak if the zero is in the left-half s-plane and as a negative peak if it is in the right-half s-plane. In the latter case the mode is unstable. Furthermore, the full width at half maximum (FWHM) of the peak is $2\mathrm{Re}(s_0)$. The simple interpretation of the spikes in $\rho(\Omega)$ must be used with care at low frequencies. Here the cut singularities of $D(s)$ on the negative s-axis, for $s \leq 1/\tau_c$, may give a negative spike in $\rho(\Omega)$ even though there are no zeros of $D(s)$ in the right-half s-plane near $s = 0$.

Fig. 13 shows $\rho(\Omega)$ as a function of $\Omega/2\pi$ for the mode 1^{I} and for three values of the pump rate (J_0/J_{th} =1.00028, 1.00153, 1.00247). The curve for $J_0/J_{\mathrm{th}} = 1.00028$ has five positive peaks corresponding to five zeros of $D(s)$ in the left-half s-plane. The relation between width and $\mathrm{Re}(s_0)$ enables us to get a rough estimate of the trajectories of the zeros in the complex s-plane or equivalently in the complex Ω-plane as shown in Fig. 14. The low frequency zero is related to the carrier relaxation frequency while the others are related to the higher order lateral modes. The relative threshold frequency of the modes are 0.18, 0.49, 0.91, and 1.46 GHz for modes m =2, 3, 4, and 5. It is seen that the zeros cross the real axis at approximately these frequencies. The second zero is the first to cross the axis and thus to generate a Hopf bifurcation. The crossing occurs approximately at $J_0/J_{\mathrm{th}} = 1.0010$. This should be compared to the saddle-node bifurcation which takes place at $J_0/J_{\mathrm{th}} = 1.005$. We can, therefore, conclude that the fundamental lateral mode 1^{I} is only stable up to 0.1% above threshold, which for our bulk device corresponds to 3 mA above threshold. We expect that using quantum-well parameters will give a similar stability range of the order of a few milli-amperes. The shift of the zeros is due to increased mode coupling for increasing current. For some systems as, e.g., external cavity lasers the mode coupling may lead to improved stability of a mode [21], but in our case the mode coupling leads to instability.

The higher order lateral modes can be analyzed by a similar procedure and it shows that the modes are unstable already from threshold. Lang *et al.* [3] suggested that the mode with highest output power is stable and is the operating mode of the laser. However, our example shows that this is not necessarily true. We have calculated the output power versus pump rate for each of the modes in Fig. 2, and for the pump rate $J_0 = 1.0049J_{\mathrm{th}}$ we find that mode 3^{I} has the highest output power. The corresponding plot of $\rho(\Omega)$ shows that the mode is unstable.

VI. Noise and Modulation Spectra

In order to calculate the small-signal noise spectra from (36) one needs to know the diffusion matrix $\boldsymbol{D}(x, s)$ in the correlation relation for $\widetilde{\boldsymbol{f}}(x, s)$

$$\left\langle \widetilde{\boldsymbol{f}}(x,s)\widetilde{\boldsymbol{f}}^{\dagger}(x',s') \right\rangle = \boldsymbol{D}(x,s)\delta(x-x')2\pi\delta(\Omega-\Omega') \tag{41}$$

where $s = j\Omega$, $s' = j\Omega'$, and "$\langle\rangle$" indicates ensemble averaging. In Appendix D we show how the diffusion matrix can be determined from the correlation relations for the Langevin noise function $F(\boldsymbol{r}, \omega)$ in (2).

The RIN spectrum, $\mathrm{RIN}(x_0, \Omega)$, at lateral coordinate x_0 is given by

$$\mathrm{RIN}(x_0,\Omega) = 4\lim_{T\to\infty}\frac{1}{T}\left\langle \left|\frac{\widetilde{\delta a}(x_0,s)}{a_s}\right|^2 \right\rangle \tag{42}$$

where the Fourier transform of $\delta a(x_0, t)$ is assumed to be taken over a time interval of duration T. The factor 4 is due to the

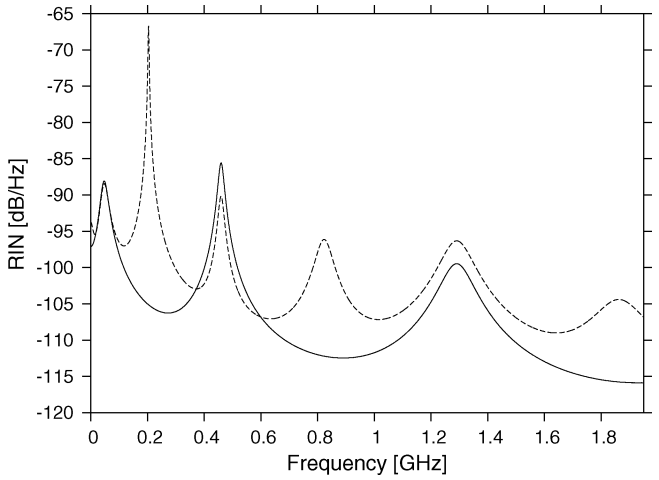

Fig. 15. RIN spectrum for the fundamental mode 1^{I} and for $J_0 = 1.0028\,J_{\mathrm{th}}$. The curves are for $x_0 = 0$ (solid) and $x_0 = -40$ μm (dashed).

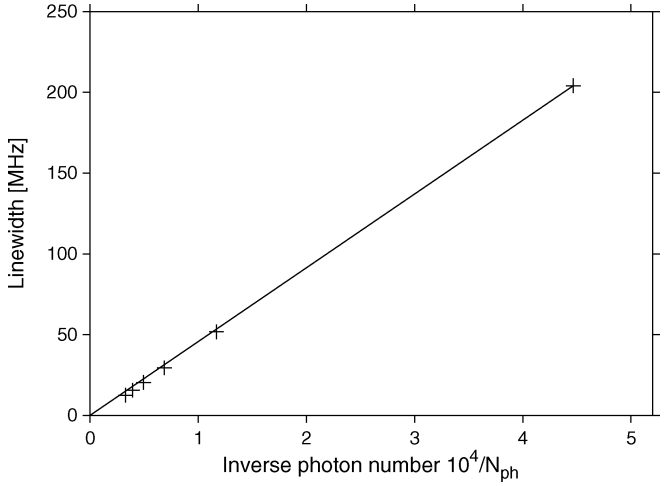

Fig. 16. Calculated linewidth versus inverse photon number for selected pump rates. The line connects the origin with the point of largest linewidth.

relative intensity change being twice the relative change $\widetilde{\delta a}/a_s$ in amplitude. The latter is given by (36) for $i = 1$ and for the purely noise driven case with $\widetilde{\boldsymbol{j}} = 0$. By insertion of (36) in (42) and using the correlation relation (41) we find

$$\mathrm{RIN}(x_0,\Omega) = 4\int_{-d}^{d} \boldsymbol{\zeta}_1^{\dagger}(x,x_0,s)\boldsymbol{D}(x,s)\boldsymbol{\zeta}_1(x,x_0,s)dx. \quad (43)$$

We obtain in a similar way an expression for the local frequency spectrum $S_{\dot\phi}(x_0,\Omega)$ by noticing that the Fourier transform of the frequency $d(\delta\phi)/dt$ is $s\widetilde{\delta\phi}$, and that $\widetilde{\delta\phi}$ is given by (36) for $i = 2$. Hence

$$\begin{aligned} S_{\dot\phi}(x_0,\Omega) &= \lim_{T\to\infty}\frac{1}{T}\left\langle\left|s\widetilde{\delta\phi}(x_0,s)\right|^2\right\rangle \\ &= \Omega^2\int_{-d}^{d}\boldsymbol{\zeta}_2^{\dagger}(x,x_0,s)\boldsymbol{D}(x,s)\boldsymbol{\zeta}_2(x,x_0,s)dx. \quad (44)\end{aligned}$$

The spectrum $\mathrm{RIN}(x_0,\Omega)$ is shown in Fig. 15 for the fundamental mode and for the current $J_0/J_{\mathrm{th}} = 1.00028$ at which the mode is still stable according to Fig. 13. The solid curve is for $x_0 = 0$ and the dashed curve is for $x_0 = -40$ μm. The peaks in the spectrum arise from the zeros of the system determinant $D(s)$ indicated by open squares in Fig. 14. For $x_0 = 0$ the spectrum only get contributions from modes of even parity.

The low frequency limit of $S_{\dot\phi}(x_0,\Omega)$ gives the spectral linewidth $\Delta\nu = S_{\dot\phi}(x_0,0)/2\pi$. However, since $\boldsymbol{\zeta}_2^{\dagger}$ is singular at $s = 0$, the limit of $s\boldsymbol{\zeta}_2^{\dagger}$ for $s \to 0$ has to be determined with care. We derive the limit in Appendix C and show that it is independent of x_0. The spectral linewidth is, therefore, also independent of x_0. Fig. 16 shows the calculated linewidth of the fundamental mode as a function of the inverse of the number of photons, N_{ph}, in the BA laser. The relationship is seen to be close to linear in this approximation where only spontaneous emission noise is included. A more precise calculation should include noise from current injection, carrier recombination and mode partition.

The local field power spectrum $S_E(x_0,\Omega)$ is the Fourier transform of the field correlation function, i.e.,

$$S_E(x_0,\Omega) = \int_{-\infty}^{\infty}\langle E^*(x_0,t)E(x_0,t+\tau)\rangle\, e^{-j\Omega\tau}d\tau. \quad (45)$$

By following the line of arguments in the appendix of [21] one derives the following approximate expression for $S_E(x_0,\Omega)$:

$$\begin{aligned} S_E(x_0,\Omega)/\left|E_s(x_0)\right|^2 &\simeq L(\Omega) + \frac{b\Omega}{\Omega^2+(\pi\Delta\nu)^2} \\ &+ \left\{(S_{\dot\phi} - 2\pi\Delta\nu)\frac{1}{\Omega^2} + S_{a\phi} - \frac{b}{\Omega} + \frac{1}{4}\mathrm{RIN}\right\}\otimes L(\Omega). \quad (46)\end{aligned}$$

The function $L(\Omega)$ is the Lorentzian

$$L(\Omega) = \frac{2\pi\Delta\nu}{\Omega^2+(\pi\Delta\nu)^2} \quad (47)$$

and the symbol "$\otimes$" means convolution in the frequency domain. $S_{a\phi}(x_0,\Omega)$ is the amplitude-phase cross-spectral density

$$\begin{aligned} S_{a\phi}(x_0,\Omega) &= \lim_{T\to\infty}\frac{2}{T}\mathrm{Im}\left\langle\left(\widetilde{\boldsymbol{\psi}}(x_0,s)\right)_1\left(\widetilde{\boldsymbol{\psi}}^*(x_0,s)\right)_2\right\rangle \\ &= 2\int_{-d}^{d}\mathrm{Im}\left\{\boldsymbol{\zeta}_1^{\dagger}(x,x_0,s)\boldsymbol{D}(x,s)\boldsymbol{\zeta}_2(x,x_0,s)\right\}dx. \end{aligned} \quad (48)$$

The spectrum diverges as $1/\Omega$ for $\Omega \to 0$ and requires special attension in a numerical calculation. We define a parameter "b" by

$$b \equiv \lim_{\Omega\to 0}\Omega S_{a\phi}(x_0,\Omega) \quad (49)$$

which means that $S_{a\phi} - b/\Omega$ is finite for $\Omega \to 0$ and can be convoluted numerically with $L(\Omega)$ without problem. The principal value of the convolution of b/Ω with $L(\Omega)$ can be derived analytically and gives the second term on the right-hand side of (46).

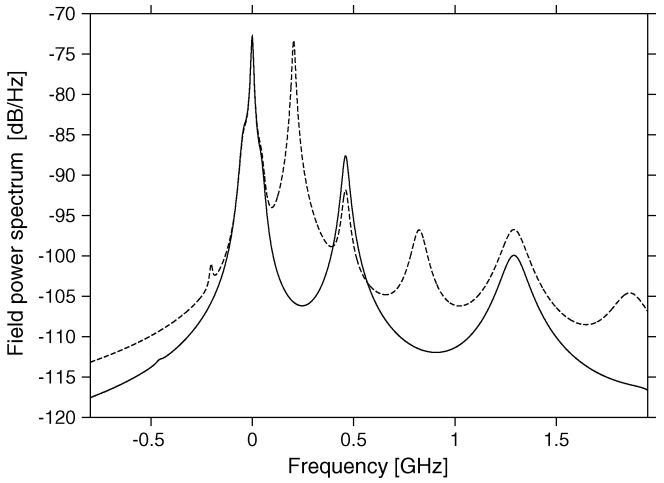

Fig. 17. Normalized field power spectrum, $S_E(x_0,\Omega)/|E_s(x_0)|^2$, for the same case as Fig. 15. The curves are for $x_0 = 0$ (solid) and $x_0 = -40\ \mu$m (dashed).

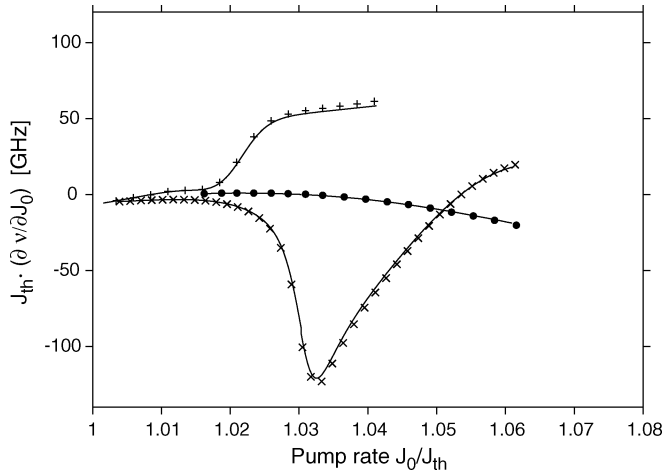

Fig. 18. Slope of the tuning curves for modes $4^{\mathrm{I}}(+)$, $7^{\mathrm{I}}(\times)$ and $15^{\mathrm{I}}(\bullet)$ obtained from (51). The solid curves are obtained by numerical differentiation of the tuning curves in Fig. 3.

Fig. 17 shows the field power spectrum of the fundamental mode for the same parameters as in Fig. 15. As expected the side modes only appear at higher frequencies compared to the fundamental mode. The asymmetry is ensured by the amplitude-phase cross-spectral density which eliminates the spikes in the RIN and frequency spectra at negative Ω due to the zeros in the systems determinant (notice again that $D(j\Omega) = D^*(-j\Omega)$). The small spike at -0.18 GHz is the four wave mixing image of the side mode at 0.18 GHz. The effect of carrier relaxation oscillations is seen as shoulders on the central peak at $\Omega = 0$. The spectral dependence on the lateral position x_0 is in qualitative agreement with the experiments in [17]. The present calculation of the field power spectrum ignores the effects of gain dispersion. This is justified when the focus is on spectral details determined by the carrier dynamics on the scale of a few GHz. In reality the BA laser oscillates in several longitudinal modes [17]. In order to calculate the full longitudinal spectrum one may introduce a field equation like (6) for each longitudinal mode.

The solution (36) also allows us to calculate the response in amplitude and frequency to a modulation $\widetilde{\delta J}(x,s)$ of the pump current. Thus, by inserting the modulation driving term (34) in (36) we get the following expression for the frequency modulation (FM) response, $\delta\nu = s\widetilde{\delta\phi}/2\pi$:

$$\delta\nu(x_0,s) = \frac{k_r\Gamma a}{2\pi}\int_{-d}^{d} s\boldsymbol{\zeta}_2^{\dagger}(x,x_0,s)\begin{pmatrix}\alpha\\-1\end{pmatrix} \cdot\frac{\tau_c\widetilde{\delta J}(x,s)}{1+s\tau_c+|E_s(x)|^2/P_{\mathrm{sat}}}dx. \quad (50)$$

The static change in frequency due to a static change $\delta J(x) = J_s(x)\delta J_0/J_0$ in the pump current can be determined from (50) by taking the limit $s \to 0$. As for the linewidth calculation this involves the low frequency limit of $s\boldsymbol{\zeta}_2^{\dagger}$, which is derived in Appendix C and which is independent of x_0. The expression for the slope of the tuning curves becomes:

$$\frac{\partial\nu}{\partial J_0} = \frac{k_r\Gamma a}{2\pi J_0}\int_{-d}^{d}\lim_{s\to 0}\left(s\boldsymbol{\zeta}_2^{\dagger}\right)\begin{pmatrix}\alpha\\-1\end{pmatrix}\cdot\frac{\tau_c J_s(x)}{1+|E_s(x)|^2/P_{\mathrm{sat}}}dx. \quad (51)$$

In Fig. 18, we have compared the slopes derived from the tuning curves in Fig. 2 with the slopes obtained from (51). The agreement between the two ways of deriving the slope gives a useful check of the numerical calculations.

VII. Discussion

We have presented a detailed analysis of the lateral modes of a solitary BA laser. In previous analyses, the focus has been on calculation of the lateral modes of definite parity, and asymmetric modes have only been calculated for BA lasers with optical feedback from an external reflector. We have traced the frequency tuning curves for the lateral modes, symmetric as well as asymmetric, as function of current pump rate. The diagram of tuning curves versus pump rate shows a pattern which suggests that the modes are categorized into four groups or types. For future work, it would be interesting to calculate how the diagram is modified and frequency degeneracies are lifted by carrier diffusion or by asymmetric pump current distributions. In the present work, we ignored the effects of carrier diffusion in order to simplify the stability analysis.

We have presented a Green's function method for determining the small-signal stability of the lateral modes. It has been suggested [3] that the mode with highest output power is stable. However, in our example it is only the fundamental mode that is stable in a narrow range of pump currents above threshold. For this mode we calculate expressions for small-signal noise and current modulation spectra. The expressions could be tested by comparison with the experimental results on the near threshold spectral distributions by Mailhot *et al.*, shown in [17, Fig. 4].

APPENDIX A
THE MEAN FIELD APPROXIMATION

In this appendix, we derive an approximate equation for the lateral variation of the field by averaging over the longitudinal coordinate z. The approximation is expected to be good when the spacing of longitudinal modes is significantly larger than the spacing of lateral modes.

Inserting (3) in the scalar wave equation (2) leads by standard procedures to the transverse field equation

$$\left[\frac{\partial^2}{\partial y^2}+k_0^2\epsilon(\mathbf{r})\right]\phi(y)=k_{\text{eff}}^2\phi(y) \tag{52}$$

and the in-plane field equations for $E_\omega^\pm(x,z)$

$$\left[\frac{\partial^2}{\partial x^2}\mp 2j\beta\frac{\partial}{\partial z}+\left(k_{\text{eff}}^2-\beta^2\right)\right]E_\omega^\pm=f_\omega^\pm \tag{53}$$

where

$$f_\omega^\pm(x,z)=\int_{-\infty}^{\infty}F(\mathbf{r},\omega)\phi^*(y)dye^{\pm j\beta z}. \tag{54}$$

The eigenvalue (52) determines the fundamental transverse mode $\phi(y)$ and the corresponding effective wave number $k_{\text{eff}}(x,z,\omega)$. We ignore the weak dependence of ϕ on x.

The mean field approximation deals with averages over the z-coordinate; an averaged variable is denoted by putting a bar over the variable. Thus

$$\overline{E_\omega^\pm}(x)=\frac{1}{l}\int_0^l E_\omega^\pm(x,z)dz. \tag{55}$$

The longitudinal average of (53) yields the equations

$$\frac{\partial^2}{\partial x^2}\overline{E_\omega^\pm}\mp\frac{2j\beta}{l}\left(E_\omega^\pm(x,l)-E_\omega^\pm(x,0)\right)+(k^2-\beta^2)\overline{E_\omega^\pm}=\overline{f_\omega^\pm} \tag{56}$$

where we have assumed that $\overline{k_{\text{eff}}^2E_\omega^\pm}=\overline{k_{\text{eff}}^2}\;\overline{E_\omega^\pm}$ and defined k by $k^2\equiv\overline{k_{\text{eff}}^2}$. The envelope fields $E_\omega^\pm$ obey the boundary conditions

$$E_\omega^+(x,0)=r_1E_\omega^-(x,0) \tag{57}$$

$$E_\omega^-(x,l)=r_2e^{-j2\beta l}E_\omega^+(x,l) \tag{58}$$

at the two end facets. With β satisfying (4) we find that (56), (57), and (58) lead to the simple equation

$$\frac{\partial^2}{\partial x^2}E_\omega+(k^2-\beta^2)E_\omega=f_\omega \tag{59}$$

for the weighted field and noise functions $E_\omega(x)$and $f_\omega(x)$ given by

$$E_\omega(x)=\frac{1}{\sqrt{2r_1}}\left(\overline{E_\omega^+}+r_1\overline{E_\omega^-}\right) \tag{60}$$

$$f_\omega(x)=\frac{1}{\sqrt{2r_1}}\left(\overline{f_\omega^+}+r_1\overline{f_\omega^-}\right). \tag{61}$$

If $E_\omega^\pm$ are independent of z, the average photon density in the active layer becomes (see [25, Appendix D])

$$S(x,t)\simeq\frac{2\epsilon_0nn_g\Gamma}{\hbar\omega h_a}K\left|E(x,t)\right|^2 \tag{62}$$

where $E(x,t)$ is given by (11), h_a is the thickness of the active layer and where we have used that $|\phi(0)|^2h_a\simeq\Gamma$. K is the longitudinal Peterman-factor [26]

$$K=\frac{(r_1+r_2)(r_1r_2-1)}{2r_1r_2ln(r_1r_2)}. \tag{63}$$

For most practical cases, the factor K is close to one. We will assume that (62) is a useful approximation even when longitudinal holeburning makes $E_\omega^\pm$ dependent on z.

The total power output P_{tot} for a stationary field distribution $E_s(x)$ is

$$P_{\text{tot}}=2\alpha_ml\epsilon_0ncK\int_{-\infty}^{\infty}\left|E_s(x)\right|^2dx. \tag{64}$$

APPENDIX B
THE GREEN'S FUNCTION $\boldsymbol{\zeta}_i(x,x_0,s)$ AND THE SYSTEM DETERMINANT $D(s)$

This appendix presents a method for calculating the Green's function $\boldsymbol{\zeta}_i(x,x_0,s)$ including a derivation of an expression for the system determinant $D(s)$.

Defining $\boldsymbol{\gamma}_i(x,x_0,s)$ by

$$\boldsymbol{\gamma}_i=\frac{d}{dx}\boldsymbol{\zeta}_i-\boldsymbol{M}_1^\dagger\boldsymbol{\zeta}_i \tag{65}$$

we can write (35) in the form

$$\frac{d}{dx}\boldsymbol{\gamma}_i+\boldsymbol{M}^\dagger\boldsymbol{\zeta}_i=\hat{\boldsymbol{e}}_i\delta(x-x_0). \tag{66}$$

For $x\neq x_0$, the two equations (65) and (66) can be written as a first-order differential equation

$$\frac{d}{dx}\boldsymbol{u}_i=\boldsymbol{M}_u\boldsymbol{u}_i \tag{67}$$

by introducing the 4-D vector $\boldsymbol{u}_i(x,x_0,s)$

$$\boldsymbol{u}_i=\begin{pmatrix}\boldsymbol{\gamma}_i\\ \boldsymbol{\zeta}_i\end{pmatrix} \tag{68}$$

and the 4×4 matrix $\boldsymbol{M}_u(x,s)$

$$\boldsymbol{M}_u=\left(\begin{array}{c|c}\boldsymbol{0} & -\boldsymbol{M}^\dagger\\ \hline \boldsymbol{I} & \boldsymbol{M}_1^\dagger\end{array}\right). \tag{69}$$

Here, $\boldsymbol{0}$ is the 2×2 null matrix and $\boldsymbol{I}$ is the 2×2 unit matrix.

Let $\boldsymbol{y}_j$, $j=1,\cdots,4$, be four linear independent solutions to the homogeneous equation $d\boldsymbol{y}/dx=\boldsymbol{M}_u\boldsymbol{y}$. The 4×4 matrix $\boldsymbol{Y}=\{\boldsymbol{y}_1,\boldsymbol{y}_2,\boldsymbol{y}_3,\boldsymbol{y}_4\}$ with columns $\boldsymbol{y}_j$ is, therefore, a solution to

$$\frac{d}{dx}\boldsymbol{Y}(x,s)=\boldsymbol{M}_u\boldsymbol{Y}(x,s). \tag{70}$$

We define $\boldsymbol{Y}$ to be the solution which is the unit matrix at $x = -d$, i.e.,

$$\boldsymbol{Y}(-d,s) = \boldsymbol{I}. \tag{71}$$

The solution to (67) can then be written as

$$\boldsymbol{u}_i(x,x_0,s) = \begin{cases} \boldsymbol{Y}(x,s)\boldsymbol{a}_i, & -d \le x < x_0 \\ \boldsymbol{Y}(x,s)\boldsymbol{b}_i, & x_0 < x \le d. \end{cases} \tag{72}$$

where $\boldsymbol{a}_i$ and $\boldsymbol{b}_i$ are 4-D vectors. From (66), it follows that

$$\lim_{\epsilon\to 0}\{\boldsymbol{\gamma}_i(x_0+\epsilon,x_0,s) - \boldsymbol{\gamma}_i(x_0-\epsilon,x_0,s)\} = \hat{\boldsymbol{e}}_i \tag{73}$$

and that $\boldsymbol{\zeta}_i(x,x_0,s)$ is continuous at $x = x_0$. By introducing 4-D unit vectors $\boldsymbol{e}_j$ with components $(\boldsymbol{e}_j)_i = \delta_{ij}$, $(i,j = 1,\ldots,4)$, the conditions for $\boldsymbol{\gamma}_i$ and $\boldsymbol{\zeta}_i$ at $x = x_0$ can be expressed simply by

$$\boldsymbol{Y}(x_0,s)(\boldsymbol{b}_i - \boldsymbol{a}_i) = \boldsymbol{e}_i \tag{74}$$

for $i = 1,2$. Similarly, the boundary conditions (37) take the form

$$\begin{aligned} \boldsymbol{e}_j^T\boldsymbol{u}_i(-d,x_0,s) &= \boldsymbol{e}_j^T\boldsymbol{a}_i = 0 \\ \boldsymbol{e}_j^T\boldsymbol{u}_i(d,x_0,s) &= \boldsymbol{e}_j^T\boldsymbol{Y}(d,s)\boldsymbol{b}_i = 0 \end{aligned} \tag{75}$$

for j =1, 2. The symbol "T" means transpose.

The conditions (74) and (75) can be reduced to the following equation for the vector $\boldsymbol{b}_i$:

$$\boldsymbol{Q}^\dagger(s)\boldsymbol{b}_i = \left(\boldsymbol{Y}^{-1}(x_0,s)\right)_{1i}\boldsymbol{e}_1 + \left(\boldsymbol{Y}^{-1}(x_0,s)\right)_{2i}\boldsymbol{e}_2 \tag{76}$$

where $\boldsymbol{Q}(s)$ is the matrix

$$\boldsymbol{Q}(s) = \left\{\boldsymbol{e}_1,\boldsymbol{e}_2,\boldsymbol{Y}^\dagger(d,s)\boldsymbol{e}_1,\boldsymbol{Y}^\dagger(d,s)\boldsymbol{e}_2\right\}. \tag{77}$$

Knowing $\boldsymbol{b}_i$ from (76), and subsequently $\boldsymbol{a}_i$ from (74), the Greens function $\boldsymbol{\zeta}_i$ is obtained from (68) and (72). It is clear from (76) that $\boldsymbol{b}_i$, and hence also $\boldsymbol{a}_i$, will contain the product $\det\boldsymbol{Y}(x_0,s)\det\boldsymbol{Q}^*(s)$ in the denominator. The complex-conjugate of the product will, therefore, appear in the expression (36) for the first-order noise perturbations. The factor $\det\boldsymbol{Y}^*(x_0,s)$ depends on x_0 (but is equal to 1 for $x_0 = -d$), so it is the factor

$$D(s) = \det\boldsymbol{Q}(s) \tag{78}$$

which determines the general stability of the considered mode and which is identified as the system determinant.

APPENDIX C
LOW-FREQUENCY LIMITS

The appendix shows that the system determinant $D(s)$ has a fixed zero at $s = 0$, and it gives an expression for the stability parameter σ defined by

$$\sigma = \frac{d}{ds}D(0). \tag{79}$$

We also derive an expression for the limit of $s\boldsymbol{\zeta}_2^\dagger(x,x_0,s)$ for $s \to 0$, which is needed to calculate the spectral linewidth and the static change in frequency as response to a static change $\delta J(x)$ in pump current.

The Hermitian conjugate of (70) gives

$$\frac{d}{dx}\boldsymbol{Y}^\dagger(x,s) = \boldsymbol{Y}^\dagger(x,s)\boldsymbol{M}_u^\dagger \tag{80}$$

and from (69) and the definition (32) of the submatrix $\boldsymbol{M}$ it follows that

$$\boldsymbol{M}_u^\dagger\boldsymbol{e}_2 = -s\frac{2k_r}{v_g}\boldsymbol{e}_3. \tag{81}$$

Hence

$$\frac{d}{dx}\boldsymbol{Y}^\dagger(x,s)\boldsymbol{e}_2 = -s\frac{2k_r}{v_g}\boldsymbol{Y}^\dagger(x,s)\boldsymbol{e}_3. \tag{82}$$

which in the limit of $s = 0$ gives

$$\frac{d}{dx}\boldsymbol{Y}^\dagger(x,0)\boldsymbol{e}_2 = 0 \tag{83}$$

i.e., $\boldsymbol{Y}^\dagger(x,0)\boldsymbol{e}_2$ is a constant vector. The initial condition $\boldsymbol{Y}^\dagger(-d,s) = \boldsymbol{I}$ implies that the vector is $\boldsymbol{e}_2$ at $x = -d$ and, therefore, $\boldsymbol{Y}^\dagger(d,0)\boldsymbol{e}_2 = \boldsymbol{e}_2$. This means that the second and the fourth column in (77) are equal for $s = 0$, and thus $D(0) = \det\boldsymbol{Q}(0) = 0$ as stated above.

The stability parameter given by (79) can be seen from (77) to be the determinant

$$\sigma = \det\left\{\boldsymbol{e}_1,\boldsymbol{e}_2,\boldsymbol{Y}^\dagger(d,0)\boldsymbol{e}_1,\frac{d}{ds}\boldsymbol{Y}^\dagger(d,0)\boldsymbol{e}_2\right\}. \tag{84}$$

We obtain an expression for the derivative in (84) by differentiating (82) with respect to s at $s = 0$. This gives

$$\frac{d}{dx}\left(\frac{d}{ds}\boldsymbol{Y}^\dagger(x,0)\boldsymbol{e}_2\right) = \frac{-2k_r}{v_g}\boldsymbol{Y}^\dagger(x,0)\boldsymbol{e}_3 \tag{85}$$

and furthermore by integration with respect to x

$$\frac{d}{ds}\boldsymbol{Y}^\dagger(d,0)\boldsymbol{e}_2 = -\frac{2k_r}{v_g}\int_{-d}^{d}\boldsymbol{Y}^\dagger(x,0)\boldsymbol{e}_3 dx. \tag{86}$$

With this result the stability parameter σ can be calculated from (84). Notice that $\boldsymbol{M}_u$ in (69) is real for $s = 0$ and hence the matrix $\boldsymbol{Y}(x,0)$ is also real.

The solution (72) shows that

$$\boldsymbol{\zeta}_2(x,x_0,s) = \left(\boldsymbol{e}_3^T\boldsymbol{Y}\boldsymbol{a}_2\right)\hat{\boldsymbol{e}}_1 + \left(\boldsymbol{e}_4^T\boldsymbol{Y}\boldsymbol{a}_2\right)\hat{\boldsymbol{e}}_2 \tag{87}$$

for $-d \le x < x_0$. For $x_0 < x \le d$ the vector $\boldsymbol{a}_2$ has to be replaced by $\boldsymbol{b}_2$. From (76) and the boundary condition (74) it can be shown that

$$\lim_{s\to 0}\left(s\boldsymbol{a}_2^\dagger\right) = \lim_{s\to 0}\left(s\boldsymbol{b}_2^\dagger\right) = \frac{1}{\sigma}\left(0,0,\boldsymbol{Y}_{14}(d,0),-\boldsymbol{Y}_{13}(d,0)\right) \tag{88}$$

where σ is the stability parameter (79). Thus

$$\lim_{s\to 0}\left(s\boldsymbol{\zeta}_2^{\dagger}(x,x_0,s)\right)=\lim_{s\to 0}\left(s\boldsymbol{a}_2^{\dagger}\right)\boldsymbol{Y}^{\dagger}\left(\boldsymbol{e}_3\hat{\boldsymbol{e}}_1^{T}+\boldsymbol{e}_4\hat{\boldsymbol{e}}_2^{T}\right). \quad (89)$$

Notice that $\boldsymbol{e}_i$ and $\hat{\boldsymbol{e}}_i$ are 4-D and 2-D unit vectors. Notice also that the limit (89) is independent of x_0.

Appendix D
The Diffusion Matrix $\boldsymbol{D}(x,s)$

The diffusion matrix $\boldsymbol{D}(x,s)$ defined by (41) originates from the Langevin driving term $F(\mathbf{r},s)$ in (2), which describes the spontaneous emission noise. We will in this appendix derive an expression for $\bar{\boldsymbol{D}}(x,s)$ based on the correlation relations for $F(\mathbf{r},\omega)$.

It has been shown by Henry [26] that $F(\mathbf{r},\omega)$ obeys the correlation relations

$$\begin{aligned}\langle F(\mathbf{r},\omega)F(\mathbf{r}',\omega')\rangle&=\langle F^*(\mathbf{r},\omega)F^*(\mathbf{r}',\omega')\rangle\\&=0\\\langle F(\mathbf{r},\omega)F^*(\mathbf{r}',\omega')\rangle&=D_F(\mathbf{r},\omega)\delta(\mathbf{r}-\mathbf{r}')2\pi\delta(\omega-\omega')\end{aligned} \quad (90)$$

where

$$D_F(\mathbf{r},\omega)=\frac{2\omega^3\hbar}{c^3\epsilon_0}ng_m n_{\mathrm{sp}}. \quad (91)$$

Here, n is the refractive index, g_m the material gain, and n_{sp} the spontaneous emission factor. They all depend on space and frequency.

From the definitions (54) and (61) of $f_\omega^{\pm}(x,z)$ and $f_\omega(x)$, it follows by (90) that

$$\begin{aligned}\langle f_\omega(x)f_{\omega'}(x')\rangle&=\langle f_\omega^*(x)f_{\omega'}^*(x')\rangle\\&=0\\\langle f_\omega(x)f_{\omega'}^*(x')\rangle&=D_f(x,\omega)\delta(x-x')2\pi\delta(\omega-\omega')\end{aligned} \quad (92)$$

where

$$D_f(x,\omega)=\frac{1}{2r_1l^2}\int_{-\infty}^{\infty}\int_0^l\left\{D_F(\mathbf{r},\omega)\,|\phi(y)|^2\times\left(r_1^2e^{\alpha_m z}+e^{-\alpha_m z}\right)\right\}dydz. \quad (93)$$

We will approximate $D_f(x,\omega)$ by

$$D_f(x,\omega)\simeq\frac{2\omega^3\hbar}{c^3\epsilon_0 l}Kn_a g n_{\mathrm{sp}} \quad (94)$$

where n_a is the refractive index in the active region, and $g=\int_{-\infty}^{\infty}g_m|\phi(y)|^2dy$ is the modal gain. All parameters n_a, g and n_{sp} are averaged over z. K is the Peterman factor (63).

The relation analogous to (11) between $f(x,t)$ and $f_\omega(x)$ leads to the following relations between $f_\omega(x)$ and the components of $\widetilde{\boldsymbol{f}}(x,s)$:

$$\begin{aligned}(\widetilde{\boldsymbol{f}})_1(x,s)&=\frac{1}{2}\left(\frac{f_{\omega_s+\Omega}(x)}{E_s(x)}+\frac{f^*_{\omega_s-\Omega}(x)}{E_s^*(x)}\right)\\(\widetilde{\boldsymbol{f}})_2(x,s)&=\frac{1}{2j}\left(\frac{f_{\omega_s+\Omega}(x)}{E_s(x)}-\frac{f^*_{\omega_s-\Omega}(x)}{E_s^*(x)}\right)\end{aligned} \quad (95)$$

where $s=j\Omega$. From the correlation relations (92) for $f_\omega(x)$ we can finally obtain correlation relations for the components of $\widetilde{\boldsymbol{f}}(x,s)$ and thereby explicit expressions for the elements of the diffusion matrix in (41). They read

$$\begin{aligned}(\boldsymbol{D})_{11}&=(\boldsymbol{D})_{22}\\&=\frac{1}{4|E_s|^2}\left(D_f(x,\omega_s+\Omega)+D_f(x,\omega_s-\Omega)\right)\\(\boldsymbol{D})_{12}&=(\boldsymbol{D})_{21}^*\\&=\frac{1}{4j|E_s|^2}\left(D_f(x,\omega_s+\Omega)-D_f(x,\omega_s-\Omega)\right).\end{aligned} \quad (96)$$

In this paper, we disregard the frequency dependence of D_f, i.e., we will use the approximation

$$\bar{\boldsymbol{D}}\simeq\frac{D_f(x,\omega_s)}{2|E_s|^2}\boldsymbol{I}. \quad (97)$$

Acknowledgment

The authors wish to thank J. Mørk, COM-DTU, and J. Buus, Gayton Photonics, for fruitful discussions.

References

[1] M. Chi, N.-S. Boegh, B. Thestrup, and P. M. Petersen, "Improvement of the beam quality of a broad-area diode laser using double feedback from two external mirrors," *Appl. Phys. Lett.*, vol. 85, no. 7, pp. 1107–1109, 2004.

[2] S. Wolff, A. Rodionov, V. E. Sherstobitov, and H. Fouckhardt, "Fourier-optical transverse mode selection in external-cavity broad-area lasers: Experimental and numerical results," *IEEE J. Quantum Electron.*, vol. 39, no. 3, pp. 448–458, Mar. 2003.

[3] R. J. Lang, A. G. Larsson, and J. G. Cody, "Lateral modes of broad area semiconductor lasers: Theory and experiment," *IEEE J. Quantum Electron.*, vol. 27, no. 3, pp. 312–320, Mar. 1991.

[4] D. Mehuys, R. J. Lang, M. Mittelstein, J. Salzman, and A. Yariv, "Self-stabilized nonlinear lateral modes of broad area lasers," *IEEE J. Quantum Electron.*, vol. 23, no. 11, pp. 1909–1920, Nov. 1987.

[5] Y. Champagne, S. Mailhot, and N. McCarthy, "Numerical procedure for the lateral-mode analysis of broad-area semiconductor lasers with an external cavity," *IEEE J. Quantum Electron.*, vol. 31, no. 5, pp. 795–810, May 1995.

[6] G. P. Agrawal, "Fast-fourier-transform based beam-propagation model for stripe-geometry semiconductor lasers: Inclusion of axial effects," *J. Appl. Phys.*, vol. 56, no. 11, pp. 3100–3109, 1984.

[7] J. Buus, "Models of the static and dynamic behavior of stripe geometry lasers," *IEEE J. Quantum Electron.*, vol. 19, no. 6, pp. 953–960, Jun. 1983.

[8] H. Adachihara, O. Hess, E. Abraham, P. Ru, and J. V. Moloney, "Spatiotemporal chaos in broad-area semiconductor lasers," *J. Opt. Soc. Amer. B*, vol. 10, no. 4, pp. 658–665, 1993.

[9] O. Hess, S. W. Koch, and J. V. Moloney, "Filamentation and beam propagation in broad-area semiconductor lasers," *IEEE J. Quantum Electron.*, vol. 31, no. 1, pp. 35–43, Jun. 1995.

[10] O. Hess and T. Kuhn, "Spatio-temporal dynamics of semiconductor lasers: Theory, modelling and analysis," *Prog. Quantum Electron.*, vol. 20, no. 2, pp. 85–179, 1996.

[11] J. Martin-Regaldo, S. Balle, and N. B. Abraham, "Modelling spatio-temporal dynamics of gain-guided multistripe and broad-area lasers," *Proc. IEE Optoelectron.*, vol. 143, no. 1, pp. 17–23, 1996.

[12] I. Fischer, O. Hess, W. Elsasser, and E. Goebel, "Complex spatio-temporal dynamics in the near-field of a broad-area semiconductor laser," *Europhys. Lett.*, vol. 35, no. 8, pp. 579–584, 1996.

[13] J. Martin-Regaldo, G. H. M. van Tartwijk, S. Balle, and M. San Miguel, "Mode control and pattern stabilization in broad-area lasers by optical feedback," *Phys. Rev. A*, vol. 54, no. 6, pp. 5386–5392, 1996.

[14] J. V. Moloney, R. A. Indik, J. Hader, and S. W. Koch, "Modeling semiconductor amplifiers and lasers: From microscopic physics to device simulation," *J. Opt. Soc. Amer. B*, vol. 16, no. 11, pp. 2023–2029, 1999.

[15] C. Simmendinger, M. Munkel, and O. Hess, "Controlling complex temporal and spatio-temporal dynamics in semiconductor lasers," *Chaos, Solitons Fractals*, vol. 10, no. 4–5, pp. 851–864, 1999.
[16] E. Gehrig and O. Hess, *Spatio-Temporal Dynamcis and Quantum Fluctuations in Semiconductor Lasers. Springer Tracts in Modern Physics 189*, 1st ed. Berlin, Germany: Springer-Verlag, 2003.
[17] S. Mailhot, Y. Champagne, and N. McCarthy, "Single-mode operation of a broad-area semiconductor laser with an anamorphic external cavity: Experimental and numerical results," *Appl. Opt.*, vol. 39, no. 36, pp. 6806–6813, 2000.
[18] S. K. Mandre, I. Fischer, and W. Elsasser, "Spatiotemporal emission dynamics of a broad-area semiconductor laser in an external cavity: Stabilization and feedback-induced instabilities," *Opt. Commun.*, vol. 244, pp. 355–365, 2005.
[19] B. Tromborg, H. E. Lassen, and H. Olesen, "Traveling wave analysis of semiconductor lasers: Modulation responses, mode stability and quantum mechanical treatment of noise spectra," *IEEE J. Quantum Electron.*, vol. 30, no. 4, pp. 939–956, Apr. 1994.
[20] A. Bogatov, P. Eliseev, and B. Sverlov, "Anomalous interaction of spectral modes in a semiconductor laser," *IEEE J. Quantum Electron.*, vol. 11, pp. 510–515, Nov. 1975.
[21] E. Detoma, B. Tromborg, and I. Montrosset, "The complex way to laser diode spectra: Example of an external cavity laser with strong optical feedback," *IEEE J. Quantum Electron.*, vol. 41, no. 2, pp. 171–181, Feb. 2005.
[22] P. K. Jakobsen, J. V. Moloney, A. C. Newell, and R. Indik, "Space-time dynamics of wide-gain-section lasers," *Phys. Rev. A*, vol. 45, no. 11, pp. 8129–8137, 1992.
[23] J. R. Marciante and G. P. Agrawal, "Spatio-temporal characteristics of filamentation in broad-area semiconductor lasers," *IEEE J. Quantum Electron.*, vol. 33, no. 7, pp. 1174–1179, Jul. 1997.
[24] G. R. Hadley, J. P. Hohimer, and A. Owyoung, "Comprehensive modeling of diode arrays and broad-area devices with applications to lateral index tailoring," *IEEE J. Quantum Electron.*, vol. 24, no. 11, pp. 2138–2152, Nov. 1988.
[25] B. Tromborg, H. Olesen, and X. Pan, "Theory of linewidth for multielectrode laser diodes with spatially distributed noise sources," *IEEE J. Quantum Electron.*, vol. 27, no. 2, pp. 178–192, 1991.
[26] C. H. Henry, "Theory of spontaneous emission noise in open resonators and its application to lasers and optical amplifiers," *J. Lightw. Tech.*, vol. 4, no. 3, pp. 288–297, Mar. 1986.

Søren Blaaberg received the M.Sc. degree in engineering physics and the Ph.D. degree from the Technical University of Denmark, Lyngby, Denmark, in 2002 and 2007, respectively.

He is now a Postdoctoral Research Fellow at the Department of Optics, Communications and Materials, COM-DTU, Technical University of Denmark. His current research interests include the physics of optical semiconductor devices and nonlinear dynamics in spatially extended systems.

Paul Michael Petersen received the M.Sc. degree in engineering and the Ph.D. degree in physics from the Technical University of Denmark, Lyngby, Denmark, in 1983 and 1986, respectively.

He has 25 years of research experience in laser physics, nonlinear optics, and optical measuring techniques and he has headed several collaborative research projects within laser physics. He is now Head of Laser Systems and Optical Materials, Risø National Laboratory, Roskilde, Denmark, and Adjunct Professor in optics at the Niels Bohr Institute, Copenhagen University, Copenhagen, Denmark.

Bjarne Tromborg was born 1940 in Give, Denmark. He received the M.Sc. degree in physics and mathematics from the Niels Bohr Institute, Copenhagen University, Copenhagen, Denmark, in 1968.

He was a University Researcher studying high-energy particle physics, and for one year a high school teacher, until he joined the research laboratory of the Danish Teleadministrations, Copenhagen, in 1979. He was Head of Optical Communications Department at Tele Danmark Research (1987–1995), Adjunct Professor at the Niels Bohr Institute (1991–2001), Project Manager in Tele Danmark R&D, (1996–1998), and took a leave of absence at Technion, Haifa, Israel in 1997. He was with COM, Technical University of Denmark, from 1999 until he retired in June 2006, most of the time as Research Professor in charge of co-ordination of modeling of components and systems for optical communications. He has coauthored a research monograph and more than 100 journal and conference papers, mostly on physics and technology of optoelectronic devices.

Prof. Tromborg received the Electro-Prize from the Danish Society of Engineers in 1981. He was Chairman of the Danish Optical Society from 1999 to 2002 and was awarded the DOPS Senior Prize 2005 by the society. He was Associate Editor of the IEEE JOURNAL OF QUANTUM ELECTRONICS from 2003 to 2006.